

Methodological refinement of the submillimeter galaxy magnification bias

Paper 0: cross-correlation function measurements

González-Nuevo J.^{1,2}, Bonavera L.^{1,2}, Cueli M. M.^{3,4}, Crespo D.^{1,2}, Casas J. M.^{1,2}

¹Departamento de Física, Universidad de Oviedo, C. Federico Garcia Lorca 18, 33007 Oviedo, Spain

²Instituto Universitario de Ciencias y Tecnologías Espaciales de Asturias (ICTEA), C. Independencia 13, 33004 Oviedo, Spain

³SISSA, Via Bonomea 265, 34136 Trieste, Italy

⁴IFPU - Institute for fundamental physics of the Universe, Via Beirut 2, 34014 Trieste, Italy

ABSTRACT

Context. The measurement of the cross-correlation function between galaxy samples is crucial to accurately assess the statistical significance of the magnification bias signal in observational data. Previous works adopted a mini-tile subsampling schema as a compromise between the different kind of bias potentially affecting the measurements. However, accurately determining the value of the integral constraint (IC) correction, which is required to obtain an unbiased estimate of the true function, can be challenging due to its dependence on factors such as the survey geometry, observational properties of the galaxy samples, and the cosmological model.

Aims. In this study, we aim to develop a new methodology to estimate the cross-correlation function and uncertainties and apply it to the analysis of magnification bias in galaxy surveys.

Methods. We adopt a new methodology that uses a statistically rigorous approach to obtain more robust measurements for constraining cosmological parameters. This approach involves using the full field area to count the number of different pairs for each field and combine them into a single estimation, reducing statistical uncertainty and accounting for the full information available in the data. To estimate the covariance matrix, we divided each field into at least five patches, and the patches were defined automatically using a k-mean clustering algorithm. For analysing individual fields, we divided them into 16 patches.

Results. We investigate the robustness of the new methodology by comparing the results from a spectroscopic lens sample with those from a photometric lens sample, finding them to be compatible. We also analyse the cross-correlation function and auto-correlation function for individual fields in the three GAMA fields, comparing the Z_{spec} and Z_{ph} samples. One of the fields, the GAMA15, was found to have a stronger signal compared to the other fields, suggesting that the stronger cross-correlation found in GAMA15 is produced by the rare combination of two excesses of large-scale structure in both the foreground and background samples.

Conclusions. Our results demonstrate the robustness of the new methodology and suggest that the differences with respect to the mini-tile approach may be due to physical properties of the samples themselves. The subsequent papers of this three-part series focus on other aspects of the study of magnification bias and will address the potential bias introduced by the GAMA15 signal to the constraint of cosmological parameters.

Key words. galaxies: high-redshift – submillimeter: galaxies – gravitational lensing: weak – cosmology: large-scale structure of Universe – methods: data analysis

1. Introduction

Magnification bias, the excess number of high-redshift sources near low-redshift mass structures, is a promising cosmological probe that can shed light on the large-scale structure of the universe and the distribution of dark matter (see Bonavera et al. 2022, and references therein). Magnification bias measurements complement other cosmological probes and provide independent constraints on cosmological parameters. This phenomenon is caused by gravitational lensing, where the distribution of matter in the universe, such as galaxies or clusters of galaxies, bends light as it travels through space, magnifying or distorting the apparent brightness and size of distant objects (see e.g., Schneider et al. 1992).

This bias can be clearly seen when two source samples that do not share the same redshift range have a significant cross-correlation function. This means that the foreground sources are magnifying the background ones. Several studies have detected

this effect in different scenarios: for example, between galaxies and quasars (Scranton et al. 2005; Ménard et al. 2010), between Herschel sources and Lyman-break galaxies (Hildebrandt et al. 2013), or between the cosmic microwave background (CMB) and other sources (Bianchini et al. 2015, 2016).

In this paper, we focus on sub-millimeter galaxies (SMGs) as background sources due to their optimal properties for lensing studies, such as their steep luminosity function, high redshifts, and faint emission in the optical band (see, for example, Blain 1996; Negrello et al. 2007, 2010, 2017; González-Nuevo et al. 2012, 2017; Bussmann et al. 2012, 2013; Fu et al. 2012; Wardlow et al. 2013; Calanog et al. 2014; Nayyeri et al. 2016; Bakx et al. 2018, 2020, among the most important ones). Several publications have demonstrated the magnification bias effect on SMGs, and it has been measured with high significance (González-Nuevo et al. 2014, 2017, 2021; Bonavera et al. 2019, 2020; Cueli et al. 2021; Fernandez et al. 2022; Crespo et al. 2022). Moreover, the ability to split the foreground sample into

different redshift bins allows for a more detailed tomographic analysis (Bonavera et al. 2021; Cueli et al. 2022).

It is worth noting that all these previous results are based on the common area between the Herschel Astrophysical Terahertz Large Area Survey (H-ATLAS; Eales et al. 2010) and the Galaxy and Mass Assembly (GAMA; Driver et al. 2011; Baldry et al. 2010, 2014; Liske et al. 2015) surveys. This common area is divided into four independent fields: GAMA09 (G09; 48.4 square degrees), GAMA12 (G12; 48.6 square degrees), GAMA15 (G15; 49.4 square degrees), and south Galactic pole (SGP; 60 square degrees). Although these fields are technically large enough to derive cosmological constraints, they are still small compared to other wide-area galactic surveys such as the Sloan Digital Sky Survey (SDSS; Blanton et al. 2017; Ahumada et al. 2019), the Dark Energy Survey (DES; The Dark Energy Survey Collaboration 2005), or the future *Euclid* (Euclid Collaboration et al. 2022). Therefore, there is a possibility that these previous results were affected by sample size limitations or sample variance statistical issues. The former occurs when the number of data points in a study is not large enough to draw accurate conclusions about the population from which the sample was drawn. Sample variance, on the other hand, measures how much the individual data points differ from the sample mean.

To minimise these effects, the most effective strategy is to increase the overall area. This is certainly possible, but there are caveats that make the transition not straightforward. For example, H-ATLAS has an additional field, the north Galactic pole or NGP, with 199.6 square degrees, but it was not covered by the GAMA survey. Several other independent surveys, such as the *Herschel* Multi-tiered Extragalactic Survey (HerMES; Oliver et al. 2012), or the Great Observatories Origins Deep Survey-*Herschel*, (GOODS-H; Elbaz et al. 2011), have observed wide fields with *Herschel*, but each of them has slightly different characteristics that need to be homogenised before being combined into a single analysis. Additionally, there is probably no single foreground survey that covers all of them. In any case, we are planning to move in that direction in the near future. However, before addressing such challenges, we would like to review the methodology used in our previous studies with well-known and established data before increasing the available area by analysing all the available *Herschel* wide area surveys.

The importance of methodology in science cannot be overstated. A well-designed and well-executed study is crucial for producing accurate, reliable, and meaningful scientific findings. By employing established methods and procedures, scientists can reduce the risk of introducing personal biases or subjective interpretations into their work. This includes scrutinising the study design, the sampling methods, data collection procedures, and statistical analyses. Reviewing the methodology of a study is vital to ensure the accuracy and validity of the results, identify potential biases, and enhance future research. A critical evaluation of the study methodology can reveal strengths and weaknesses, leading to recommendations for modifications that can improve the accuracy and reliability of future research.

Our initial plan was to write a single manuscript covering the main aspects of the magnification bias measurement and analysis, but as we delved into the details, it became apparent that the topic was too complex for a single manuscript. Therefore, we decided to split our work into a three-part series, with each paper focusing on a particular aspect related to the study of magnification bias.

The paper concentrates on the measurement itself of the cross-correlation function and its uncertainties. This aspect is of fundamental importance to accurately assess the statistical sig-

nificance of the magnification bias signal in the observational data. The paper provides a detailed description of a new methodology used to measure the cross-correlation function, along with an in-depth analysis of the sources of uncertainty. It also proposes strategies to mitigate these uncertainties and improve the accuracy of the measurements.

The first official paper, (Paper I; Cueli et al. 2024), assesses the cosmological performance of the submillimeter galaxy magnification bias with the new data that come out from this paper using a single foreground redshift bin. Particular focus is made on theoretical aspects and assumptions and numerical approximations that may affect the results with a view to extending the framework to future galaxy samples.

The second official paper focuses on the tomographic case (Paper II; Bonavera et al. 2024), which involves optimising the CPU time and strategies as well as the selection of different redshift bins. This aspect is particularly relevant for studies that involve a large number of redshift bins and a high computational load. The paper proposes several strategies to optimise the CPU time while maintaining a high level of accuracy in the measurements. It also discusses the impact of the selection of different redshift bins on the final results.

The three papers constitute a comprehensive and in-depth analysis of the different aspects involved in the study of magnification bias on submillimeter galaxies. They provide a detailed methodology for measuring the cross-correlation function and reducing uncertainties, a theoretical framework for interpreting the observational data, and strategies to optimise the computational load and the selection of redshift bins.

This paper is structured as follows: Sect. 2 describes the data used in the analysis. Sect. 3 details the measurement methodology employed to quantify the magnification bias effect. The estimation of uncertainties is discussed in Sect. 4. Sect. 5 investigates the robustness of the measurements and tests their potential sample variance. Finally, Sect. 6 summarises the main conclusions.

2. Data

2.1. Background sample

The H-ATLAS is the largest extragalactic survey conducted by the *Herschel* space observatory (Pilbratt et al. 2010), covering an extensive area of approximately 610 square degrees. The Photodetector Array Camera and Spectrometer (PACS; Poglitsch et al. 2010) and the Spectral and Photometric Imaging Receiver (SPIRE; Griffin et al. 2010) instruments were utilised in the survey, which spanned the wavelength range between 100, μm and 500, μm . Detailed information on the H-ATLAS map-making, source extraction, and catalogue generation can be found in Ibar et al. (2010), Pascale et al. (2011), Rigby et al. (2011), Valiante et al. (2016), Bourne et al. (2016), and Maddox & Dunne (2020).

The background sample for this study was derived from H-ATLAS sources detected in the three GAMA survey fields (total common area of ~ 147 square degrees), NGP, and the part of SGP that overlaps with the spectroscopic foreground sample. We applied a photometric redshift selection of $1.2 < z < 4.0$ to avoid any overlap in the redshift distributions of lenses and background sources, leaving us with $\sim 66,000$ sources ($\sim 24\%$ of the initial sample and $\langle z_{\text{ph}} \rangle = 2.20$). The redshift estimation is described in detail in González-Nuevo et al. (2017) and Bonavera et al. (2019). This background sample is identical to the one used in previous works (González-Nuevo et al. 2014,

2017, 2021; Bonavera et al. 2019, 2020, 2021; Cueli et al. 2021, 2022; Fernandez et al. 2022; Crespo et al. 2022).

The redshift distribution of the background sources used in our analysis (represented by the red line in Fig. 1) is estimated as $p(z|W)$ for galaxies selected by our window function, which is a top hat function for the redshift range of $1.2 < z < 4.0$. This distribution takes into account the effect of random errors in photometric redshifts, following the methodology described in González-Nuevo et al. (2017). In that work, it is demonstrated that the potential contamination of lower-redshift sources ($z < 0.8$) with photometric redshifts above 1.2 is statistically negligible, even when accounting for the uncertainties in photometric redshift estimation (see González-Nuevo et al. 2017, and references therein).

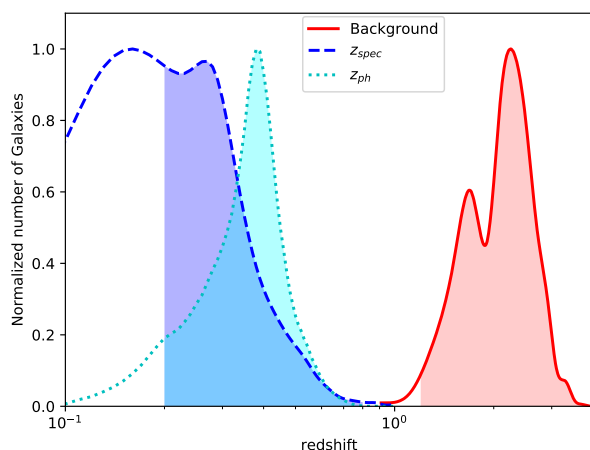


Fig. 1. Normalised redshift distributions of the three catalogues used in this work: the background sample, that is H-ATLAS high- z SMGs (solid red line); the GAMA spectroscopic foreground sample (dashed dark blue line); and the SDSS photometric foreground sample (dotted light blue line).

2.2. Foreground samples

This study utilises two distinct foreground samples, each selected independently. The first sample, is the default one employed in previous works (González-Nuevo et al. 2021; Bonavera et al. 2020, 2021; Cueli et al. 2021, 2022) and is referred to as the " z_{spec} sample". This sample comprises approximately 150,000 galaxies in the range of $0.2 < z_{spec} < 0.8$ (with a median value of $z_{spec} = 0.28$; see dark blue shadowed region in Fig. 1), obtained from the GAMA II spectroscopic survey (Driver et al. 2011; Baldry et al. 2010, 2014; Liske et al. 2015). The H-ATLAS and GAMA II surveys were selected to maximise their overlap, covering the three equatorial regions at 9, 12, and 14.5 h (referred in this work as G09, G12, and G15, respectively) and the SGP one. The total common area used in this study was approximately 207 square degrees, considering only the regions where both surveys overlap.

The second foreground sample was obtained from the 16th data release of the Sloan Digital Sky Survey (SDSS; Blanton et al. 2017; Ahumada et al. 2019), consisting of galaxies with photometric redshift within the range of $0.2 < z_{ph} < 0.8$ and photometric redshift error $z_{err}/(1+z) < 1$ (photoErrorClass = 1). This sample, called the " z_{ph} sample," covers a total area of approximately 317 square degrees, encompassing the H-ATLAS equa-

torial regions and the NGP, and includes roughly 962,000 galaxies in the common area, with a median value of $z_{ph} = 0.38$ (see light blue shadowed region in Fig. 1). The second sample was introduced to investigate the impact of increasing the density of potential lenses on the measurements and their robustness with respect to the use of different foreground samples.

3. Methodology aspects

3.1. Tiling schema

The H-ATLAS survey used a scanning strategy that resulted in overlapping rhomboidal shapes, or "tiles," in most fields, each covering an area of approximately 16 square degrees. However, as outlined in the detailed analysis by González-Nuevo et al. (2021), dividing the full area in smaller "mini-tiles" produces more robust cross-correlation measurements with fewer required corrections. Mini-tiles are obtained by dividing a tile into four equal parts, each covering approximately 4 square degrees, which are then adapted to the field limits. As the size of the mini-tiles is similar to the angular distances we would like to study, the only required correction is the Integral Constraint (IC), which we discuss in detail in Sect. 3.3. Examples of mini-tile shapes and sizes are shown by the red squares in Figs. 2 and 3. The use of mini-tiles was also the default tiling scheme in previous related works, such as Bonavera et al. (2020, 2021) and Cueli et al. (2021, 2022).

In this work, we revisit the conclusions of González-Nuevo et al. (2021) regarding measurement strategies for the H-ATLAS fields. According to their study, the mean value of the measurements taken using the full area of each field have smaller uncertainties and do not require an Integral Constraint (IC) correction. However, this approach was disregarded due to an additional large angular scale bias that is difficult to correct. Because of its advantages, we explore the possibility of using the overall available area in our study and investigate the nature and impact of the large angular scale bias.

Even if the mini-tile scheme is not used for the measurement itself, a subdivision of all the available area into minimal subregions is still necessary to assign meaningful uncertainties to the measurement and, more generally, to estimate the covariance matrix, as discussed in Sect. 4. However, using mini-tiles poses a practical challenge as the vertices of each of them must be manually defined. While this task was accomplished for the four H-ATLAS fields with 63 mini-tiles, it becomes increasingly time-consuming when expanding the study to other wide field surveys observed by Herschel, which could have hundreds of mini-tiles. To address this issue, we have adopted a more flexible subregion definition procedure that maintains similar properties to the previous definition but is more scalable for future studies.

To define the subregions, we drew inspiration from the methodology used by TreeCorr, a popular software package for measuring galaxy clustering (Jarvis 2015). TreeCorr uses a k-means clustering algorithm to partition the data into subregions known as 'patches,' which are similar in size and shape to our mini-tiles. Specifically, we adopted the k-means algorithm provided by the SciPy library. The algorithm aims to minimise the sum of squared distances between data points and their assigned centroid. To determine the number of clusters (i.e., the patches), we imposed a minimum area for each cluster. We added an additional step by repeating the procedure 10 times with different random initial centroids, and selecting the run that yielded the most consistent number of data points across different clusters.

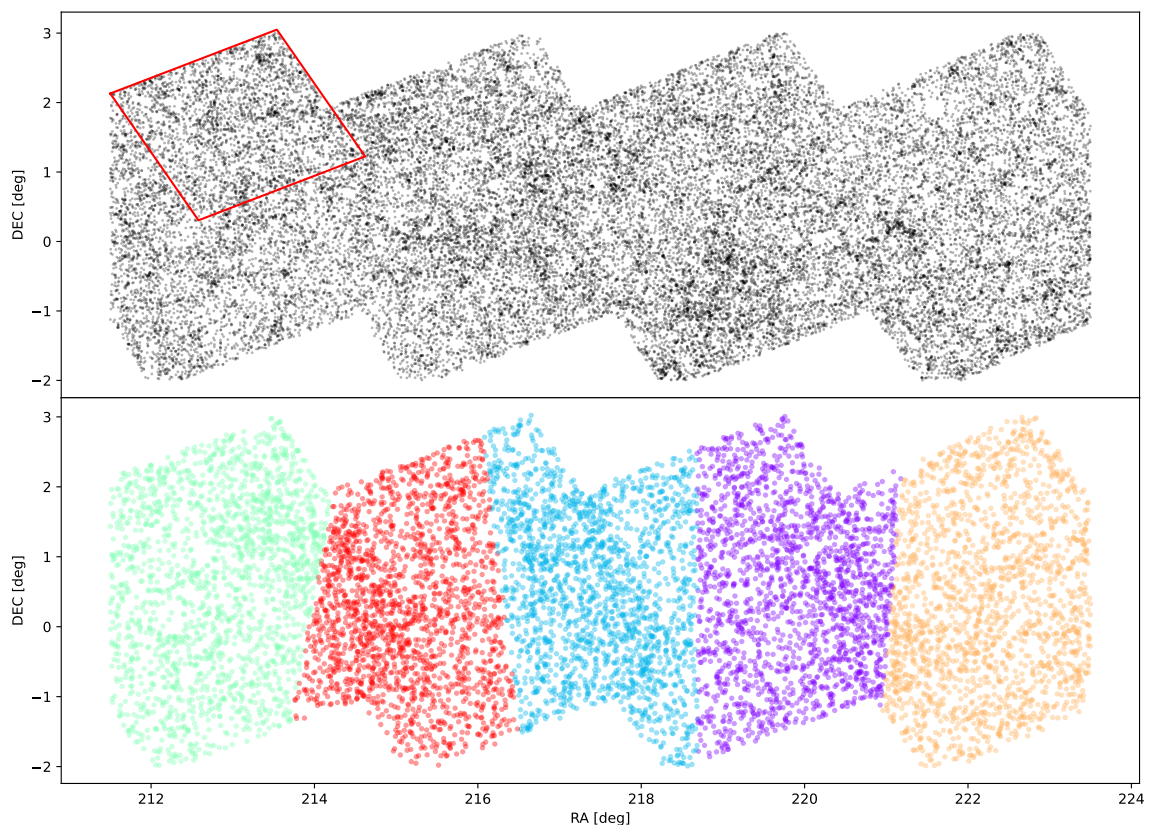


Fig. 2. The spatial distribution of foreground (top panel) and background (bottom panel) sample galaxies for the G15 field. For the background sample, different colours indicate patch definitions, with five of them shown (approximately 9.6 square degrees each). The red square in the top panel indicates the typical shape and size of a "mini-tile" (see text for more details).

Figures 2 and 3 show the distribution of foreground (top panels) and background (bottom panels) sample galaxies for the G15 and G09 fields, respectively. Different colours are used to indicate examples of patch definitions, with five clusters (approximately 9.6 square degrees each) shown for the G15 and 16 clusters (approximately 3 square degrees each) shown for the G09. The particular number of clusters is related to the estimation of the covariance matrix and will be discussed in Sect. 4. Due to the specific limits of the field, clusters with smaller areas tend to adopt more regular shapes.

3.2. Auto/Cross-correlation estimators

The angular auto-correlation function $w_{\text{auto}}(\theta)$ is estimated with the Landy-Szalay estimator (Landy & Szalay 1993),

$$\hat{w}_{\text{auto}}(\theta) = \frac{DD(\theta) - 2DR(\theta) + RR(\theta)}{RR(\theta)}, \quad (1)$$

where DD, DR and RR are the normalised data-data, data-random and random-random pair counts for a given angular separation θ .

On the other hand, as described in detail in González-Nuevo et al. (2017) and Bonavera et al. (2020), the cross-correlation function measurement is performed via a modified version of

the Landy & Szalay (1993) estimator (Herranz 2001),

$$\hat{w}_{\text{fb}}(\theta) = \frac{D_f D_b(\theta) - D_f R_b(\theta) - D_b R_f(\theta) + R_f R_b(\theta)}{R_f R_b(\theta)}, \quad (2)$$

where $D_f D_b$, $D_f R_b$, $D_b R_f$ and $R_f R_b$ are the normalised foreground-background, foreground-random, background-random and random-random pair counts for a given angular separation θ .

The instrumental noise caused by the scanning strategy leads to a surface density variation in the background galaxy sample (see Fig. 2 and more clearly in Fig. 4, top panel, of González-Nuevo et al. 2021). The overlap between the tiles reduces such noise and allows fainter sources to be detected. To correct for this bias, we generated random catalogues using the same procedure as in Amvrosiadis et al. (2019): a flux is randomly chosen using the cumulative probability distribution of fluxes of the real sources. Then, a random position on the image is generated, and the local noise is estimated as the quadratic sum of the instrumental noise in that pixel and the confusion noise. The source is kept if its flux, perturbed by a Gaussian deviate equal to the total local noise estimate, was greater than 4σ ; otherwise, the process is repeated starting from choosing a flux randomly.

After accounting for the instrumental noise variation, we observed a slight decrease in the cross-correlation function at the

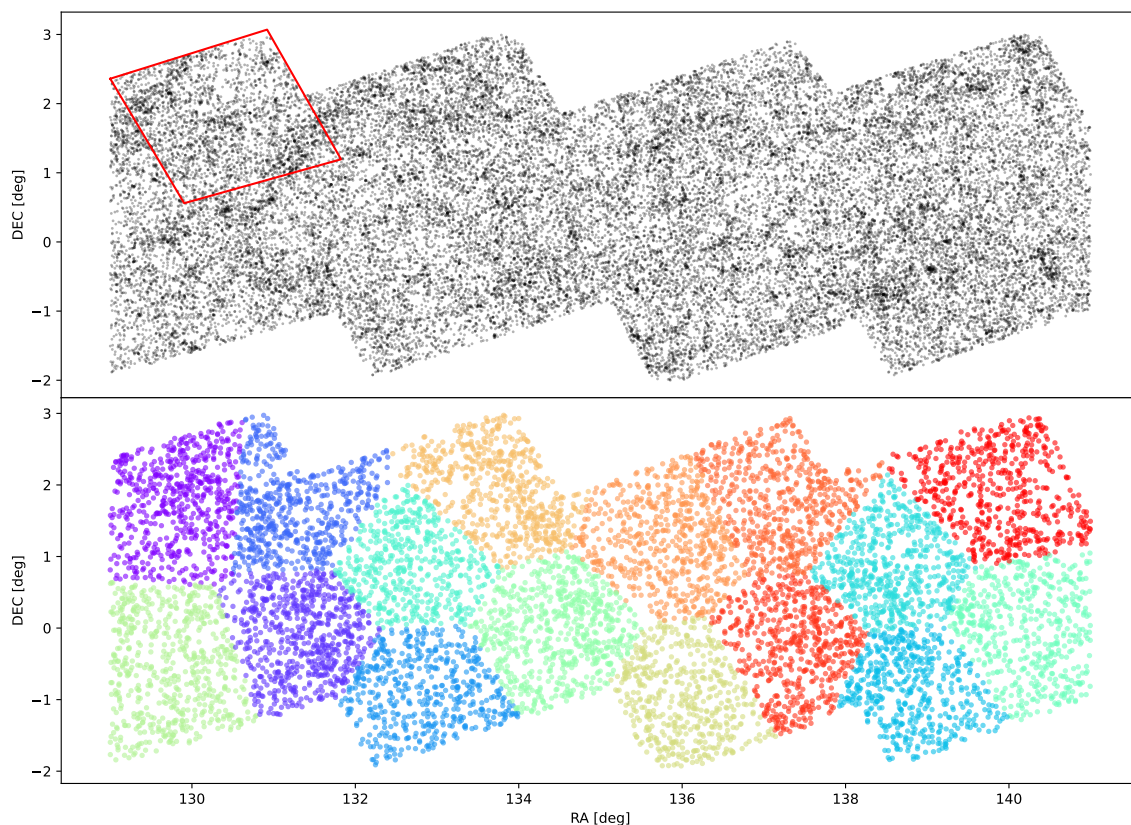


Fig. 3. The spatial distribution of foreground (top panel) and background (bottom panel) sample galaxies for the G09 field. For the background sample, different colours indicate patch definitions, with 16 of them shown (approximately 3 square degrees each). The red square in the top panel indicates the typical shape and size of a "mini-tile" (see text for more details).

largest angular scales. This kind of correction is not needed for the foreground galaxy samples.

In the case of the mini-tiles schema, as in previous works, we compute the angular (auto-)cross-correlation function for each mini-tile. To ensure stability, we average over ten different realisations, each using different random catalogues. To minimise cosmic variance, we compute the mean value of the cross-correlation functions estimated in each selected area for a given angular separation bin. The uncertainties are computed as the standard error of the mean, $\sigma_{\mu} = \sigma / \sqrt{n}$, where σ is the standard deviation of the population and n is the number of independent areas. Each selected region is assumed to be statistically independent due to the minimal overlap.

In González-Nuevo et al. (2021), the authors also compute the mean value of the four cross-correlation functions estimated in each entire field area and the standard error of the mean as its uncertainty. In this work, we adopted a more statistically rigorous approach by counting the number of different pairs for each field and combining them into a single estimation. This method accounts for the full information available in the data and reduces the statistical uncertainty compared to measuring four separate (auto-)cross-correlation functions. However, when more independent fields become available in the future, the two approaches are expected to converge to similar results due to the

increased statistical power and reduced sample variance. The uncertainties associated to this approach will be discussed in detail in Sect. 4.

3.3. IC discussion

When averaging over multiple fields, the observed correlation function can be weakened at larger scales due to large-scale fluctuations. This leads to a bias in the estimated (auto-) cross-correlation function, where the "true" measurement, $\hat{w}_{\text{ideal}}(\theta)$ is related to the observed measurement $\hat{w}(\theta)$ by a constant that is precisely the IC, i.e.

$$\hat{w}_{\text{ideal}}(\theta) = \hat{w}(\theta) + \text{IC}. \quad (3)$$

There are theoretical approaches to estimate the IC for a particular scanning strategy (see e.g., Adelberger et al. 2005), but in practice, it is commonly estimated numerically using RR counts. Specifically, the IC can be estimated for the cross-correlation using the formula:

$$\text{IC} = \frac{\sum_i R_f R_b(\theta_i) w_{\text{ideal}}(\theta_i)}{\sum_i R_f R_b(\theta_i)}, \quad (4)$$

where $w_{\text{ideal}}(\theta)$ is an assumed model for the cross-correlation function. An equivalent expression is used for the auto-correlation.

In González-Nuevo et al. (2021), a power-law model is assumed $w_{\text{ideal}}(\theta) = A\theta^{-\gamma}$, where A and γ are the best-fit parameters for the power law using only the observed cross-correlation function below 20 arcmin. For the mini-tiles, the derived IC value is 9×10^{-4} .

However, as illustrated in Fig. 4, the estimation of the IC correction is more complex than it may seem. The cross-correlation function derived using the entire available area (shown as red circles), which can be considered unbiased with respect to the IC, differs from the mini-tiles one (black circles even below 10 arcmin after the above IC value is applied). Therefore, if the IC is estimated using the measurements from the whole available area, the IC value would be larger due to the lower steepness of the cross-correlation function.

Moreover, the power-law approach is simply an effective approximation of the halo model (as described in detail in paper II). If we estimate the IC assuming the theoretical halo model as the true model in Eq. (3), but restricting to angular separations < 10 arcmin, mostly unaffected by the cosmological model, it will underestimate the IC correction. On the other hand, if we include also the largest angular separations, the estimated IC correction can be affected by the cosmological model assumed. This means that the choice of angular separation limit becomes arbitrary, biased or model-dependent, which should be avoided. Even more, the largest angular scales are the most important for constraining cosmological parameters, but they are also the most influenced by the adopted IC correction when using the mini-tile schema.

We attempted various methods to refine the IC value. Firstly, we conducted a polynomial fit analysis using the two sets of measurements, i.e., the mini-tiles, which were expected to be biased low, and the whole area measurements, which were likely biased high, as discussed later. The polynomial fit analysis yielded two extreme values for the IC: 7 and 18×10^{-4} . These limits defined the range of IC values that were compatible with our measurements.

To avoid the choice of an angular separation limit, we performed a power-law fit that included a constant value, the IC correction. However, most of the algorithms we tested were unable to converge to a solution. The derived IC value was 13×10^{-4} , which was in agreement with the previously defined range. Nevertheless, it was not possible to estimate a robust uncertainty for this value.

Next, we used theoretical estimates of the halo model (see paper II for details about the theoretical model) to account for all angular scales but avoiding the power-law shape, specially at large angular scales where the model should decline. To restrict the astrophysical parameters and to be as independent as possible from the considered cosmological model, we followed this analysis. Firstly, we performed a Maximum Likelihood Estimation (MLE) search for the astrophysical parameters using only the 1-halo range measurements and random uniform cosmological parameters. With these astrophysical parameters, we obtained the IC distribution for another 100 random uniform cosmological parameter sets, resulting in a mean value of 15×10^{-4} with a dispersion of 13×10^{-4} . However, several cosmologies were found to be incompatible with our data, so we further restricted them to those providing IC values in the range of $7 - 18 \times 10^{-4}$, resulting in a mean value of 11×10^{-4} and a dispersion of 3×10^{-4} .

To test the sensitivity of our results to the assumed cosmological parameter distribution, we repeated the analysis using Gaussian random cosmological parameter sets based on the Planck

ones (Planck Collaboration et al. 2020) with a larger dispersion, ~ 0.05 . This resulted in a mean IC value of 13×10^{-4} and a dispersion of 4×10^{-4} . Again, restricting the IC values to the range of $7 - 18 \times 10^{-4}$, we obtained a mean value of 13×10^{-4} and a dispersion of 2×10^{-4} .

After considering the different cases, we selected a round number that fell between the most precise cases with a larger sigma. We choose a final IC value of 12×10^{-4} with a dispersion of 3×10^{-4} as the most appropriate IC estimate for our study using the mini-tile schema, taking into account the range of results obtained from various analyses and assumptions.

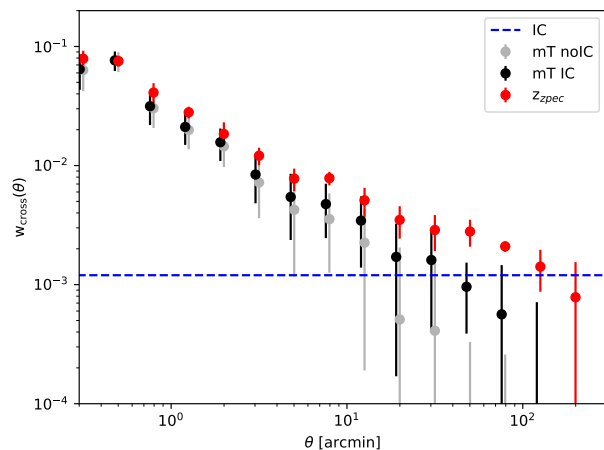


Fig. 4. Comparison of the cross-correlation function estimated using different approaches. Grey circles correspond to the mini-tile approach before the IC correction is applied (see blue dashed line). Black circles correspond to the mini-tile results after the IC correction, while red circles are estimated using the new approach without any further correction. The uncertainties are derived from the covariance matrices.

Figure 4 provides a comparison of the cross-correlation function estimated using different approaches. Grey circles represent the mini-tile results before the IC correction, which show a sharp decline above 10 arcmin (where the blue dashed line, representing the IC correction, becomes relevant). Black circles correspond to the mini-tile results after applying the IC correction, while the red ones are estimated using the new approach without any further correction. The uncertainties are derived from the covariance matrices, which is described in the next section.

The mini-tile results are consistent with the new results within the uncertainties up to 30 arcmin, but they appear to be slightly underestimated across all angular scales. Above 30 arcmin, which are the most important for cosmological constraints, the new results are clearly higher than the mini-tile ones. However, the precise behaviour of the mini-tile results at these larger angular scales depends on the specific value of the IC correction, which also depends on the cosmological model. Therefore, such methodology should be avoided if there is a better alternative as the one proposed in this work. When considering higher IC values, such as $IC = 15 - 20 \times 10^{-4}$, the two measurements become compatible even at the largest angular separations.

4. Covariance estimation

4.1. Definitions

Covariance matrices are widely used in astronomy to estimate the uncertainties of measurements. In simple terms, a covari-

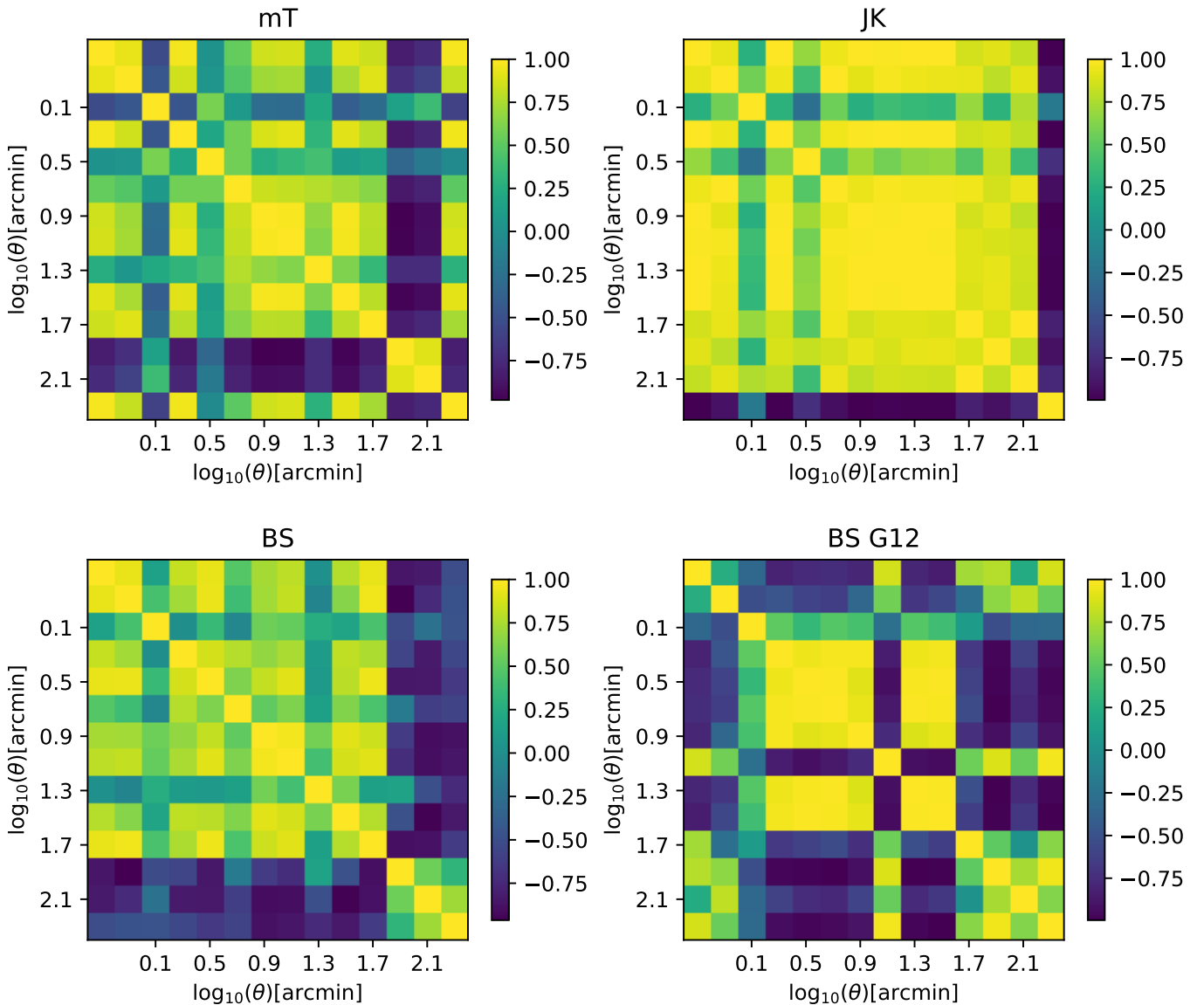


Fig. 5. Comparison of the correlation matrices estimated with three methods for the cross-correlation signal. The mini-tiles estimation (top left) and the bootstrapping estimation (bottom left) are similar, with higher correlation at central angular distances. However, the Jackknife estimation (top right) shows strong correlation across all angular separations, indicating an implementation issue. To address potential signal variation among fields, the covariance matrix is estimated for each individual field using 16 patches of approximately three square degrees each (bottom panel; example for the G12 field).

ance matrix quantifies the degree of correlation between different measured quantities. Moreover, the covariance matrix provides information on the degree of coherence in the data, which can be used to identify potential sources of systematic errors or to optimise the design of future astronomical surveys.

Let's assume we have a sample of size N_s of m independent random variables, $\{X_1, \dots, X_m\}$. The covariance matrix can be estimated using the usual sample covariance formula, that is,

$$\text{Cov}(x_i, x_j) = \frac{1}{N_s - 1} \sum_{k=1}^{N_s} (x_i^k - \bar{x}_i)(x_j^k - \bar{x}_j), \quad (5)$$

where x_i^k and \bar{x}_i are the k -th observation and the sample mean of the variable x_i . The factor $\frac{1}{N_s - 1}$ in the formula is called

Bessel's correction and is used to correct for the bias in the sample covariance matrix due to estimating the population mean from the sample.

This covariance matrix estimation is the natural choice when the measurement is obtained as the average of several independent observations and it is commonly known as 'subsampling'. However, it is clear that this approach cannot be used when only a single measurement is available, as it is our case using the whole available area. Moreover, according to Norberg et al. (2009), the subsampling approach assumes that the subsamples used for estimating the covariance matrix are independent of each other, which is often not the case in galaxy clustering studies due to the presence of long-range modes in density fluctuations. This correlation between subsamples arises from the non-zero value of the correlation function at large scales. Therefore,

alternative internal estimators need to be considered that can account for these limitations.

Jackknife and bootstrapping are alternative approaches based on 'resampling'. Jackknife is a leave-one-out method (Shao 1986) where subsamples of the data are created by removing one observation at a time, resulting in N subsamples with $N - 1$ data points each. The covariance matrix is then estimated as:

$$\text{Cov}(x_i, x_j) = \frac{N-1}{N} \sum_{k=1}^N (x_i^k - \bar{x}_i)(x_j^k - \bar{x}_j), \quad (6)$$

where x_i^k is the k -th Jackknife observation of the random variable X_i and \bar{x}_i is the mean of all Jackknife observations of the same random variable. The factor $\frac{N-1}{N}$ is included to take into account the fact that the resamplings of the data are not independent.

Bootstrap, on the other hand, involves randomly resampling the data N_b times with replacement to create multiple subsamples of a given size N (Efron 1979). The covariance matrix is then estimated as the sample covariance matrix of the subsamples, which can be written as:

$$\text{Cov}(x_i, x_j) = \frac{1}{N_b} \sum_{k=1}^{N_b} (x_i^k - \bar{x}_i)(x_j^k - \bar{x}_j), \quad (7)$$

where x_i^k is the observation of the random variable X_i coming from the k -th Bootstrap sample and \bar{x}_i is the average over all N_b Bootstrap samples.

Both Jackknife and Bootstrap are non-parametric approaches, meaning that they do not require any assumptions about the underlying distribution of the data. The choice between the two methods depends on the nature of the data and the research question at hand.

4.2. Practical considerations

In our case, the m random variables described in the above section are the angular (auto-)cross-correlation function at different angular scales. However, one practical issue that arises when dealing with spatial data is that the naive method of resampling individual points (galaxies) does not work in this context. When subsampling spatial data, it is important to preserve the underlying dependence structure as much as possible in order to obtain valid estimates (Norberg et al. 2009). Thus, instead of resampling individual galaxies, the available area should be divided into sub-regions, and subsamples can be obtained by randomly selecting sub-regions rather than individual galaxies. This approach ensures that the subsamples retain the spatial dependence structure of the original data, which is crucial for accurate estimation of the covariance matrix and other spatial statistics.

In essence, this means that, for the subsample method, we split the area into $N_s = 63$ subregions (minitiles) and measure the auto/cross-correlation in each of those subregions, so that x_i^k is interpreted, in this case, as the auto/cross-correlation measurement at angular scale θ_i from the subregion k , that is, $\tilde{w}^k(\theta_i)$. This is the method used in previous works (Bonavera et al. 2020, 2021; González-Nuevo et al. 2021; Cueli et al. 2021, 2022). However, for the Jackknife and Bootstrap methods, we generate N different subregions according to the previously described k -means algorithm and x_i^k is to be interpreted as the auto/cross-correlation measurement at angular scale θ_i from either the k -th Jackknife subsample (that is, removing that k -th area) or the k -th Bootstrap subsample.

For any subsampling method, to avoid a singular covariance matrix estimate, we need to ensure that the number of subsamples is sufficiently large relative to the number of measurements. The Johnson-Lindenstrauss lemma provides a mathematical justification for this requirement (Achlioptas 2003). The mini-tiles schema, which uses $N_s=63$ subsamples versus 14 measurements, automatically satisfies this requirement. However, for other resampling methods, this implies that the natural subdivision into just the 4 fields may not be sufficient.

At the same time, it is important to balance the size of the sub-regions with their representativeness of the dataset. Larger sub-regions may decrease the correlation between sub-regions and the influence of pairs crossing between sub-regions, but they may also introduce bias if the sub-regions are not representative of the overall dataset. However, increasing the size of the sub-regions reduces the number of subsamples that can be obtained, which increases the variance of the covariance estimator and may require a larger number of subsamples to obtain a reliable estimate (Friedrich et al. 2016).

Finally, internal covariance estimation is valid only in the limit where the correlations between sub-regions are small. When this is the case, the sub-sample covariance matrix becomes a rescaling of the sample covariance matrix of independent realisations of the sub-regions, which allows us to estimate the covariance matrix of the full dataset. However, when the correlations between sub-regions are large, the sub-sample covariance matrix may not accurately represent the covariance matrix of the full dataset, which can lead to biased estimates (Friedrich et al. 2016).

4.3. Internal covariance matrix estimations

In light of the practical considerations discussed earlier, we chose to divide the fields into patches of approximately nine square degrees, resulting in a total of $N=22$ patches, as described in Sect. 3.1. The bottom panel of Fig. 2 shows the five patches defined for the G15 field.

For our leave-one-out Jackknife method implementation, we remove one patch from the data and estimate the cross-correlation with the remaining area in each iteration. This approach minimises potential effects on the spatial dependence structure of the original data, since we do not modify three of the fields in each iteration. Furthermore, this speeds up the calculations as the number of pairs for each field can be stored and reused between iterations. In essence, we have $N = 22$ Jackknife subsamples, which we plug into (6) to compute the associated covariance matrix.

In our Bootstrap implementation, we generate bootstrapped samples by randomly selecting, with repetition, a certain number of patches between the available ones. While the typical number of patches should be N , that is, 22 in our case, following Norberg et al. (2009), we over-sampled by a factor of 3, resulting in a total of 66 patches in this case. We confirmed their conclusion that the estimated covariance matrix using over-sampling is more robust. We generated $N_b=10000$ bootstrapped subsamples and found that increasing this number did not yield any significant improvement in the covariance matrix estimation, computed by plugging the measurements derived from the subsamples into (7).

For ease of comparison, we chose to display the correlation matrices instead of the covariance matrices since they are directly related. The correlation matrices estimated with the three methods are compared in Figure 5. The mini-tiles estimation (top left) is very similar to the bootstrapping estimation (bottom left),

but noisier. In both cases, the central angular distances (in arcmin and on a logarithmic scale) show higher correlation than the rest, corresponding to the transition between the 1- and 2-halo regimes. For the mini-tiles estimation, we added the uncertainty of the IC correction in quadrature to the diagonal of the covariance matrix.

However, the Jackknife estimation (top right) is markedly different from the other methods. It shows a strong correlation between all angular separations, indicating a problem with the implementation. As we will discuss in the next section, there exists a signal variation between the different fields that violates the validity condition for the internal covariance estimation in this particular implementation. The other estimations are less affected by this issue due to the fact that they are based on smaller and more homogeneous regions. Considering that we prefer to avoid the mini-tile approach because its strong dependence on the IC value and the worse performance of the Jackknife estimation, we adopted the bootstrapping one as our default approach to estimate the covariance matrices.

To study the potential variation of the cross-correlation signal among the different fields, we need to estimate the covariance matrix for each individual field. In those cases, we increased the number of patches per field to 16, which provides an area of approximately three square degrees per patch, even smaller than the mini-tiles. The bottom panel of Fig. 3 displays the 16 patches defined for the G09 field. The IC correction is not an issue for the covariance estimation for the mini-tiles method and the bootstrapping one, with 22 patches or the 16-patch approach, because it is cancelled in the covariance matrices calculation.

In the case of individual fields, both the bootstrapping and jackknife methods produced similar results due to the higher homogeneity between the patches. To maintain consistency, we adopted the bootstrapping method as our default to estimate the covariance matrices in all cases. Therefore, the error bars displayed in Figure 4 are simply the square root of the diagonal terms of the covariance matrices for the mini-tiles and bootstrapping methods, respectively.

5. Robustness and sample variance

We investigate the robustness of our results by applying the new methodology to a new lens sample obtained from the photometric SDSS catalogue (described in Sect. 2), and comparing the resulting cross-correlation function with that measured from the Z_{spec} sample. The measurements from the Z_{spec} sample (red circles, top panel) and the Z_{ph} one (blue circles, bottom panel) are plotted against the IC-corrected mini-tiles measurements in Fig. 6. In line with the findings of González-Nuevo et al. (2021), both samples produce compatible measurements, but the Z_{ph} measurements are slightly higher at 30-40 arcmin and do not exhibit positive cross-correlation values above 100 arcmin. However, the two measurements are clearly above the mini-tiles ones for angular separations greater than 10 arcmin, as previously mentioned. The excess using different tiling approaches with respect the mini-tiles case was interpreted as a large-scale bias by González-Nuevo et al. (2021). It is important to note that the large-scale behaviour of the mini-tile measurements depends strongly on the IC correction applied, which in turn depends on the assumed cosmological parameters.

Furthermore, the GAMA sample used in our study comes from a spectroscopic survey, which is fundamentally different from our photometric SDSS sample. Therefore, any large-scale discrepancies between the two sets of measurements cannot be

attributed to systematic errors related to the survey characteristics. Instead, it suggests that the differences may be due to physical properties of the samples themselves, such as the distribution of foreground or background galaxies, in the regions being probed. We will further investigate the nature of this discrepancy to determine whether it is a bias or a consequence of spatial variance within the samples.

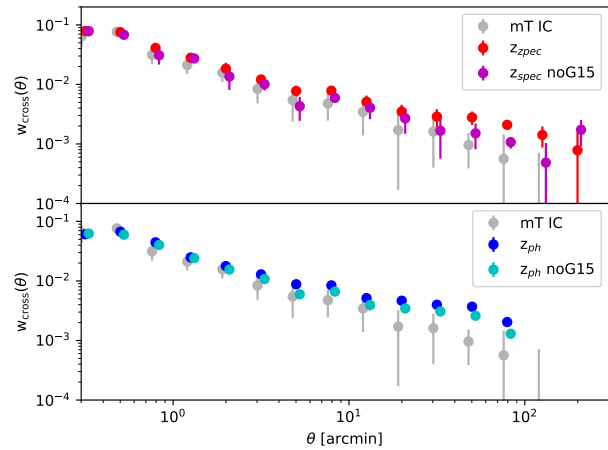


Fig. 6. Comparison of the cross-correlation function measurements from the Z_{spec} and Z_{ph} lens samples with the IC-corrected mini-tiles measurements (common in both panels, gray circles). The top panel shows the measurements from the Z_{spec} sample (red circles) and without the G15 field (magenta circles), while the bottom panel shows the measurements from the Z_{ph} sample (blue circles) and without the G15 field (cyan circles).

5.1. Sample variance

We estimated the cross-correlation function for each individual field, and the uncertainties were derived using a covariance matrix estimated using 16 patches per field. The Z_{spec} sample covers the G09, G12, G15, and SGP regions, while the Z_{ph} sample excludes SGP and includes the NGP region instead. The results for each sample are compared in Fig. 7, where the red circles represent the Z_{spec} sample and the blue circles represent the Z_{ph} sample. The mini-tiles measurements for the whole area using the Z_{spec} sample are the same in each panel and are added as a visual guide.

Focusing on the Z_{spec} sample results, we observed that the measurements for the G09, G12, and SGP fields were mostly compatible with the mini-tile measurements. However, the G15 field showed a stronger signal compared to the other fields at almost all angular separation distances. Although the SGP field showed a hint of a stronger signal above 50 arcmin, it had the worst stability and errors.

Similar conclusions were drawn from the Z_{ph} sample results. We observed a stronger signal above 30 arcmin for the G09 and G12 fields, which was not compensated for by the slightly lower signal for the NGP field. In contrast to the Z_{spec} results, no positive correlation was observed above 100 arcmin in any field with the Z_{ph} sample. These data points showed a rebound effect and, in general, had larger error bars.

Therefore, the observed stronger signal on large scales, compared to the mini-tiles case, was primarily produced by the G15 region in the Z_{spec} sample, while it was also present in the G09

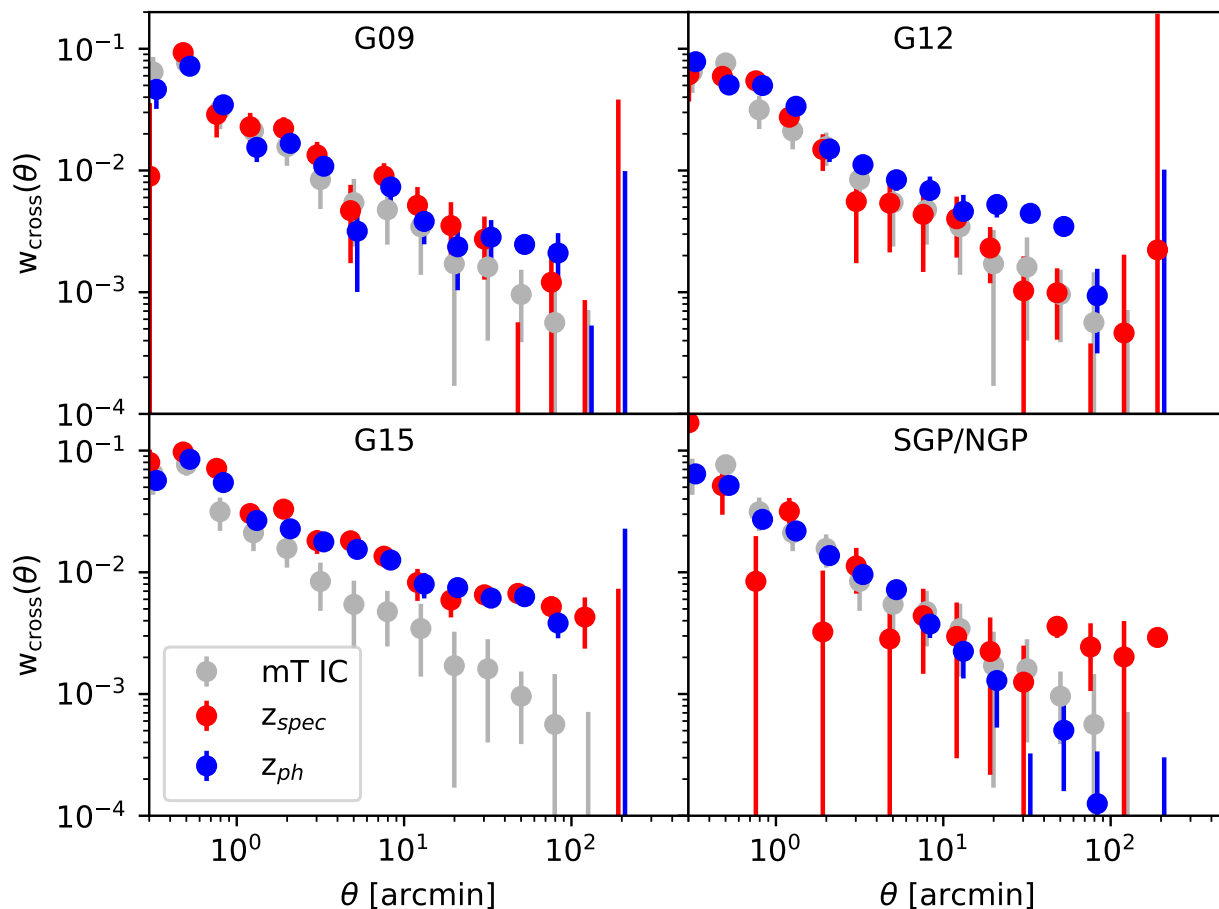


Fig. 7. Comparison of the cross-correlation functions estimated for each individual field for the spectroscopic sample (z_{spec} ; red circles) and the photometric one (z_{ph} ; blue circles). The mini-tiles measurements for the whole area are the same in each panel and are added as a visual guide (gray circles).

and G12 fields of the z_{ph} sample, albeit to a lesser extent. These findings suggest that the discrepancy is not indicative of a general large-scale bias caused by the sample or methodology, as interpreted by González-Nuevo et al. (2021), but rather it may be attributed to a sample variance issue related to the large-scale structure in the G15 region. Notably, when the G15 region is excluded from the cross-correlation estimation (see Fig. 6), the discrepancy is mitigated for the z_{spec} sample, but it persists for the z_{ph} sample.

Several studies have investigated the scale of isotropy in the galaxy distribution. Marinoni et al. (2012) analyzed luminous red galaxies from the SDSS DR7 and found a scale of isotropy at $150 h^{-1}$ Mpc, while Sarkar et al. (2019) indicated a transition to isotropy at a scale of approximately $200 h^{-1}$ Mpc for both SDSS photometric and spectroscopic data. These findings support the notion that the galaxy distribution in the local Universe is isotropic on scales larger than $200 h^{-1}$ Mpc, affirming the validity of assuming isotropy on large scales. However, considering that the typical physical scales of our fields are below $200 h^{-1}$ Mpc at the mean redshift of the samples, it is expected that sample variance plays a role in the observed discrepancies.

Sample variance arises when the small-scale structures across different regions of the universe are not perfectly cor-

related with each other, leading to variations in the large-scale structures that we observe. In order to test this hypothesis, we study the statistical properties of the samples, both foreground and background. A visual comparison between the galaxy distribution of G15 (see Fig. 2) and G09 (see Fig. 3) shows no significant difference: for the foreground sample (top panels) both regions show an equivalent amount of large-scale structure, and for the background ones, the only interesting aspect is the overlapping regions that are common in all the fields and are already taken into account in the random catalogues.

For a more quantitative analysis, we estimate the auto-correlation function for all the fields (black circles) and compare them to the ones derived from individual fields (red circles). We repeat the same analysis for both the foreground (see Fig. 8) and background samples (see Fig. 9). The cross-correlation function estimated for each individual field is also plotted as a comparison (grey circles).

As expected, the auto-correlation function from the whole area displayed the typical smooth shape with no apparent transition between the 1- and 2-halo regimes and is stronger than the cross-correlation function. We compared the auto-correlation functions estimated from each individual field and found that the regions had compatible auto-correlation values for sep-

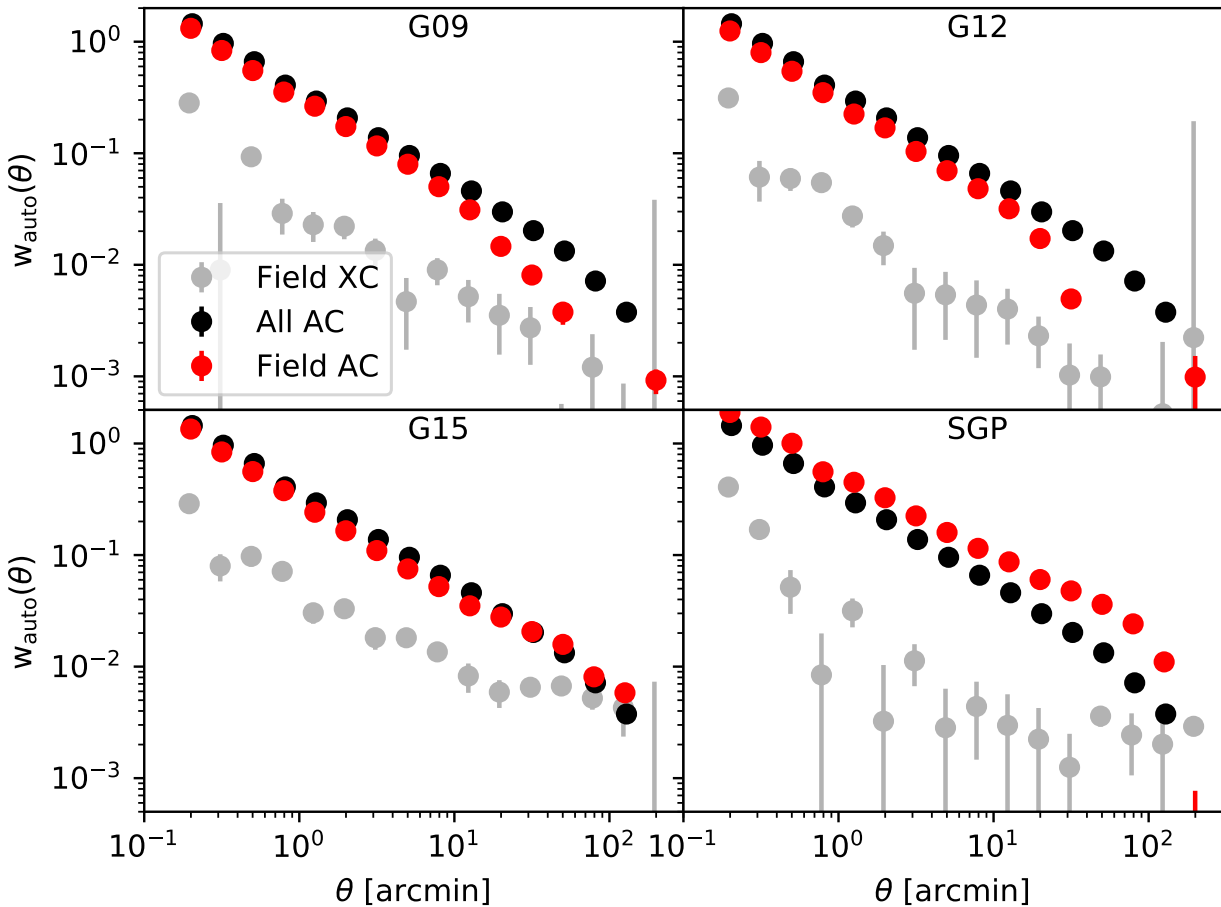


Fig. 8. The auto-correlation functions for the z_{spec} foreground sample estimated for all the fields (black circles) are compared to the ones derived from individual fields (red circles) in this figure. The cross-correlation functions estimated for each individual field are also shown for comparison (grey circles).

arations below 10 arcmin, with the SGP region showing a slightly stronger correlation. However, the behaviour of the auto-correlation function for large scales varied between the regions.

For instance, the auto-correlation function for G15 maintained a linear behaviour (in logarithmic scale) until it became negative beyond 100 arcmin, while the auto-correlation function for G09 and G12 clearly declined before such an angular separation. This result is interesting because the auto-correlation function measured for the same GAMA sample (Sureshkumar et al. 2021) and the most general SDSS one (Zehavi et al. 2005) show no decline at least until 200-300 arcmin, suggesting that G09 and G12 are regions with less large-scale structure compared to G15, which is not anomalous in this sense.

On the other hand, the SGP region displayed a clear excess compared to the other regions, indicating an excess of large-scale structure in the SGP and G15 fields compared to the G09 and G12 fields. This suggests that the particular behaviour of our lensing results in the G15 field is likely due to the presence of the stronger large-scale structure. However, the cross-correlation function for the SGP region was much weaker than for G15, indicating that this excess alone cannot explain the observed lensing results.

In the case of the background sample, the auto-correlation functions derived from the different regions are in relatively good agreement. The auto-correlation functions are estimated above 0.4 arcmin due to the beam size of Herschel detectors, and they become negative above 50 arcmin due to the angular distance dependence with redshift.

Overall, the auto-correlation function for the G15 region is very similar to those of the G09 and G12 regions, showing only slightly higher correlation. In contrast, the SGP region shows a much weaker auto-correlation function. This suggests that the anomalous behaviour of G15 may be explained by a combination of a stronger large scale structure in both the foreground and background samples. It is important to note that this is in contrast to the SGP region, which shows a stronger signal in the foreground sample but a much weaker one in the background sample.

6. Conclusions

In this study, we have developed a new methodology to estimate the cross-correlation function and uncertainties, and have applied it to the analysis of magnification bias in galaxy surveys. The study of magnification bias is a complex and multifaceted

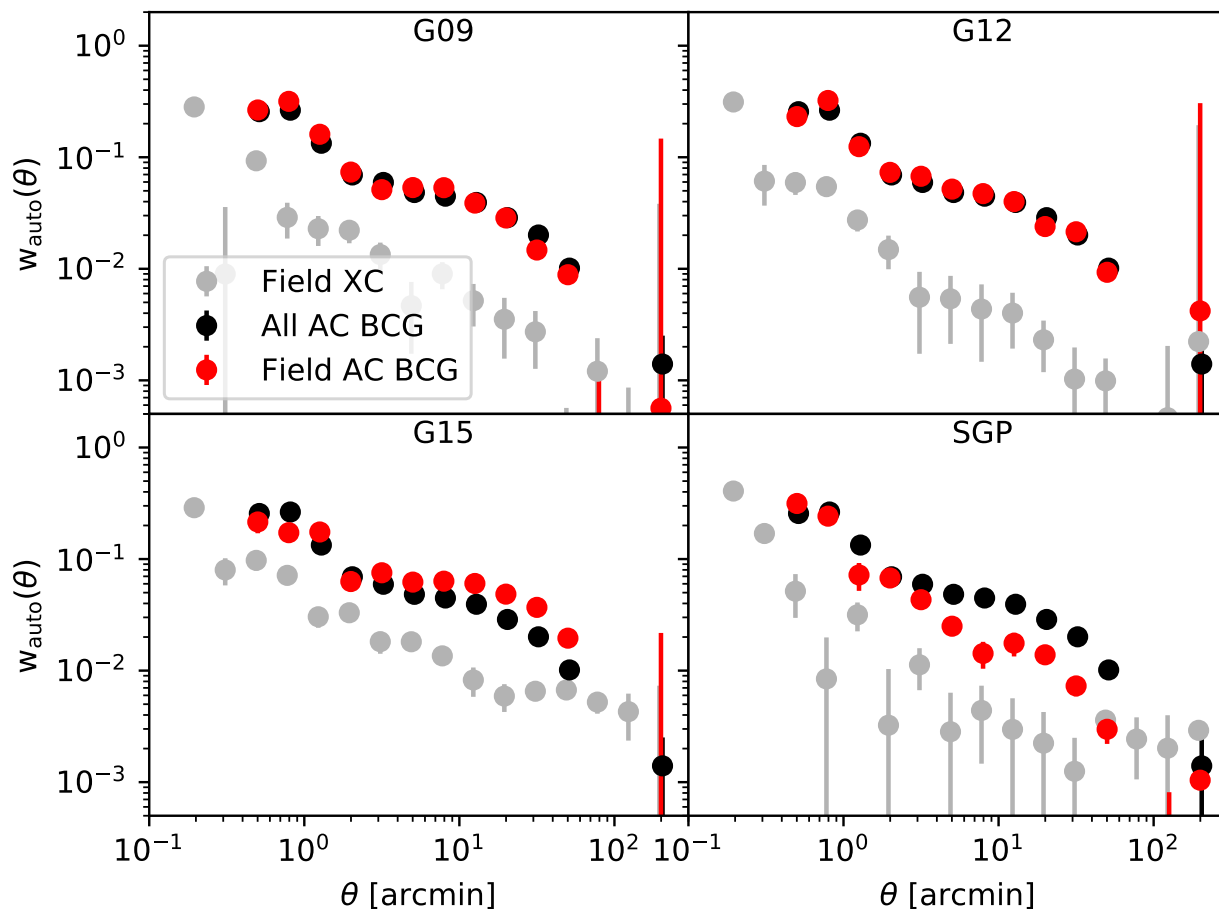


Fig. 9. The auto-correlation functions for the background sample estimated for all the fields (black circles) are compared to the ones derived from individual fields (red circles) in this figure. The cross-correlation functions estimated for each individual field are also shown for comparison (grey circles).

topic that requires a comprehensive analysis to fully understand its different aspects, in particular the methodology. As we delved into the details, it became apparent that the topic was too complex for a single paper. Therefore, we decided to split our work into a three-part series, with each paper focusing on a particular aspect related to the study of magnification bias (Cueli et al. 2024; Bonavera et al. 2024). This first paper concentrates on the measurement of the cross-correlation function and uncertainties, which is crucial to accurately assess the statistical significance of the magnification bias signal in observational data.

The mini-tiles schema has been widely used to estimate the cross-correlation function between galaxy samples, thanks to its computational efficiency and accuracy in measuring the angular clustering of galaxies. However, large-scale fluctuations can introduce a bias into the estimated cross-correlation function, and an integral constraint (IC) term is required to obtain an unbiased estimate of the true function. This correction is particularly crucial for constraining cosmological parameters on the largest angular scales. However, accurately determining the value of the IC correction can be challenging due to its dependence on factors such as the survey geometry, observational properties of the galaxy samples, and the cosmological model. In light of these

challenges, we have adopted a new methodology to obtain more robust measurements for constraining cosmological parameters.

The new methodology to estimate the cross-correlation function involves a statistically rigorous approach that uses the full field area to count the number of different pairs for each field and combine them into a single estimation. This method reduces statistical uncertainty and accounts for the full information available in the data, in contrast to measuring separate (auto-)cross-correlation functions for each field. To estimate the covariance matrix we adopted a bootstrap method by dividing each field in at least five patches, the minimum number to maximise the patches area but maintaining a number greater than the number of measurements. The patches were defined automatically using a k-mean clustering algorithm. This resampling approach ensures that the subsamples retain the spatial dependence structure of the original data. For analysing individual fields we divided them in 16 patches, instead. The new measurements were demonstrated to be more robust and with much lower uncertainties.

We investigate the robustness of the new methodology for measuring the cross-correlation function by comparing the new results from a spectroscopic lens sample with those from a photometric lens sample, i.e. they have completely different system-

atics. The measurements from both samples were found to be compatible, suggesting that the differences with respect the mini-tile approach may be due to the complexity of computing the integral constraint in a consistent manner, but also to the physical properties of the samples themselves given the behaviour of the large-scale fall.

We analyse the cross-correlation function and auto-correlation function for individual fields in the GAMA regions, comparing the z_{spec} and z_{ph} samples. The G15 field was found to have a stronger signal compared to the other fields at almost all angular separation distances for both the z_{spec} and z_{ph} samples. The results suggest that there is no general large-scale bias produced by the sample or methodology, but rather, it may be more related to a sample variance problem of the large scale structure at the G15 region. In fact, the SGP and G15 regions showed excess large-scale structures in the foreground sample compared to the G09 and G12 regions. However, this excess alone could not explain the observed lensing results because the SGP showed a weaker cross-correlation signal. Considering the background sample, the auto-correlation function for the G15 region was very similar to those of the G09 and G12 regions, showing only slightly higher correlation, while the SGP region showed a much weaker auto-correlation function. Therefore, it seems that the stronger cross-correlation found in G15 is produced by the rare combination of two excess of large-scale structure in both the foreground and background samples.

Despite the stronger signal, there is currently no indication that the G15 region should be discarded, and with the addition of more independent regions in future analyses, it will be possible to perform a statistical analysis to quantify the degree of anomaly in the G15 results. The subsequent papers of this three-part series focus on other aspects of the study of magnification bias and will address the potential bias introduced by the G15 signal to the constraint of cosmological parameters.

Acknowledgements. JGN, LB, DC, JMC acknowledge the PID2021-125630NB-I00 project funded by MCIN/AEI/10.13039/501100011033/FEDER, UE. JMC also acknowledges financial support from the SV-PA-21-AYUD/2021/51301 project.

We deeply acknowledge the CINECA award under the IS CRA initiative, for the availability of high performance computing resources and support. In particular the projects ‘SIS22_lapi’, ‘SIS23_lapi’ in the framework ‘Convenzione triennale SISSA-CINECA’.

The Herschel-ATLAS is a project with Herschel, which is an ESA space observatory with science instruments provided by European-led Principal Investigator consortia and with important participation from NASA. The H-ATLAS web-site is <http://www.h-atlas.org>. GAMA is a joint European- Australasian project based around a spectroscopic campaign using the Anglo- Australian Telescope. The GAMA input catalogue is based on data taken from the Sloan Digital Sky Survey and the UKIRT Infrared Deep Sky Survey. Complementary imaging of the GAMA regions is being obtained by a number of independent survey programs including GALEX MIS, VST KIDS, VISTA VIKING, WISE, Herschel-ATLAS, GMRT and ASKAP providing UV to radio coverage. GAMA is funded by the STFC (UK), the ARC (Australia), the AAO, and the participating institutions. The GAMA web-site is: <http://www.gama-survey.org/>.

Funding for the Sloan Digital Sky Survey IV has been provided by the Alfred P. Sloan Foundation, the U.S. Department of Energy Office of Science, and the Participating Institutions. SDSS-IV acknowledges support and resources from the Center for High-Performance Computing at the University of Utah. The SDSS web site is www.sdss.org. SDSS-IV is managed by the Astrophysical Research Consortium for the Participating Institutions of the SDSS Collaboration including the Brazilian Participation Group, the Carnegie Institution for Science, Carnegie Mellon University, the Chilean Participation Group, the French Participation Group, Harvard-Smithsonian Center for Astrophysics, Instituto de Astrofísica de Canarias, The Johns Hopkins University, Kavli Institute for the Physics and Mathematics of the Universe (IPMU) / University of Tokyo, the Korean Participation Group, Lawrence Berkeley National Laboratory, Leibniz Institut für Astrophysik Potsdam (AIP), Max-Planck-Institut für Astronomie (MPIA Heidelberg), Max-Planck-Institut für Astrophysik (MPA Garching), Max-Planck-Institut für Extraterrestrische Physik (MPE), National Astronomical Observatories of China, New Mexico State University, New York

University, University of Notre Dame, Observatório Nacional / MCTI, The Ohio State University, Pennsylvania State University, Shanghai Astronomical Observatory, United Kingdom Participation Group, Universidad Nacional Autónoma de México, University of Arizona, University of Colorado Boulder, University of Oxford, University of Portsmouth, University of Utah, University of Virginia, University of Washington, University of Wisconsin, Vanderbilt University, and Yale University.

This research has made use of the python packages *ipython* (Pérez & Granger 2007), *matplotlib* (Hunter 2007) and *Scipy* (Jones et al. 2001).

References

- Achlioptas, D. 2003, *Journal of Computer and System Sciences*, 66, 671, special Issue on PODS 2001
- Adelberger, K. L., Steidel, C. C., Pettini, M., et al. 2005, *ApJ*, 619, 697
- Ahumada, R., Allende Prieto, C., Almeida, A., et al. 2019, arXiv e-prints, arXiv:1912.02905
- Amvrosiadis, A., Valiante, E., González-Nuevo, J., et al. 2019, *Monthly Notices of the Royal Astronomical Society*, 483, 4649
- Bakx, T. J. L. C., Eales, S., & Amvrosiadis, A. 2020, *MNRAS*, 493, 4276
- Bakx, T. J. L. C., Eales, S. A., Negrello, M., et al. 2018, *MNRAS*, 473, 1751
- Baldry, I. K., Alpaslan, M., Bauer, A. E., et al. 2014, *MNRAS*, 441, 2440
- Baldry, I. K., Robotham, A. S. G., Hill, D. T., et al. 2010, *MNRAS*, 404, 86
- Bianchini, F., Bielewicz, P., Lapi, A., et al. 2015, *ApJ*, 802, 64
- Bianchini, F., Lapi, A., Calabrese, M., et al. 2016, *ApJ*, 825, 24
- Blain, A. W. 1996, *MNRAS*, 283, 1340
- Blanton, M. R., Bershad, M. A., Abolfathi, B., et al. 2017, *AJ*, 154, 28
- Bonavera, L., Cueli, M. M., & González-Nuevo, J. 2022, *Proceedings of the MG16 Meeting on General Relativity*, R. Ruffini & G. Vereshchagin eds., World Scientific., arXiv:2112.02959
- Bonavera, L., Cueli, M. M., González-Nuevo, J., et al. 2021, *A&A*, 656, A99
- Bonavera, L., Cueli, M. M., González-Nuevo, J., Casas, J. M., & Crespo, D. 2024, arXiv e-prints, arXiv:2305.13836
- Bonavera, L., González-Nuevo, J., Cueli, M. M., et al. 2020, *A&A*, 639, A128
- Bonavera, L., González-Nuevo, J., Suárez Gómez, S. L., et al. 2019, *J. Cosmology Astropart. Phys.*, 2019, 021
- Bourne, N., Dunne, L., Maddox, S. J., et al. 2016, *MNRAS*, 462, 1714
- Bussmann, R. S., Gurwell, M. A., Fu, H., et al. 2012, *ApJ*, 756, 134
- Bussmann, R. S., Pérez-Fournon, I., Amber, S., et al. 2013, *ApJ*, 779, 25
- Calanog, J. A., Fu, H., Cooray, A., et al. 2014, *ApJ*, 797, 138
- Crespo, D., González-Nuevo, J., Bonavera, L., et al. 2022, *A&A*, 667, A146
- Cueli, M. M., Bonavera, L., González-Nuevo, J., et al. 2022, *A&A*, 662, A44
- Cueli, M. M., Bonavera, L., González-Nuevo, J., & Lapi, A. 2021, *A&A*, 645, A126
- Cueli, M. M., González-Nuevo, J., Bonavera, L., et al. 2024, arXiv e-prints, arXiv:2305.13835
- Driver, S. P., Hill, D. T., Kelvin, L. S., et al. 2011, *MNRAS*, 413, 971
- Eales, S., Dunne, L., Clements, D., et al. 2010, *PASP*, 122, 499
- Efron, B. 1979, *The Annals of Statistics*, 7, 1
- Elbaz, D., Dickinson, M., Hwang, H. S., et al. 2011, *A&A*, 533, A119
- Euclid Collaboration, Scaramella, R., Amiaux, J., et al. 2022, *A&A*, 662, A112
- Fernandez, L., Cueli, M. M., González-Nuevo, J., et al. 2022, *A&A*, 658, A19
- Friedrich, O., Seitz, S., Eifler, T. F., & Gruen, D. 2016, *MNRAS*, 456, 2662
- Fu, H., Jullo, E., Cooray, A., et al. 2012, *ApJ*, 753, 134
- González-Nuevo, J., Cueli, M. M., Bonavera, L., et al. 2021, *A&A*, 646, A152
- González-Nuevo, J., Lapi, A., Bonavera, L., et al. 2017, *J. Cosmology Astropart. Phys.*, 2017, 024
- González-Nuevo, J., Lapi, A., Fleuren, S., et al. 2012, *ApJ*, 749, 65
- González-Nuevo, J., Lapi, A., Negrello, M., et al. 2014, *MNRAS*, 442, 2680
- Griffin, M. J., Abergel, A., Abreu, A., et al. 2010, *A&A*, 518, L3
- Herranz, D. 2001, in *Cosmological Physics with Gravitational Lensing*, ed. J. Tran Thanh Van, Y. Mellier, & M. Moniez, 197
- Hildebrandt, H., van Waerbeke, L., Scott, D., et al. 2013, *MNRAS*, 429, 3230
- Hunter, J. D. 2007, *Computing In Science & Engineering*, 9, 90
- Ibar, E., Ivison, R. J., Cava, A., et al. 2010, *MNRAS*, 409, 38
- Jarvis, M. 2015, *TreeCorr: Two-point correlation functions*, Astrophysics Source Code Library, record ascl:1508.007
- Jones, E., Oliphant, T., Peterson, P., et al. 2001, *SciPy: Open source scientific tools for Python*
- Landy, S. D. & Szalay, A. S. 1993, *ApJ*, 412, 64
- Liske, J., Baldry, I. K., Driver, S. P., et al. 2015, *Monthly Notices of the Royal Astronomical Society*, 452, 2087
- Maddox, S. J. & Dunne, L. 2020, *MNRAS*, 493, 2363
- Marinoni, C., Bel, J., & Buzzi, A. 2012, *J. Cosmology Astropart. Phys.*, 2012, 036
- Ménard, B., Scranton, R., Fukugita, M., & Richards, G. 2010, *MNRAS*, 405, 1025
- Nayeri, H., Keele, M., Cooray, A., et al. 2016, *ApJ*, 823, 17

- Negrello, M., Amber, S., Amvrosiadis, A., et al. 2017, MNRAS, 465, 3558
Negrello, M., Hopwood, R., De Zotti, G., et al. 2010, Science, 330, 800
Negrello, M., Perrotta, F., González-Nuevo, J., et al. 2007, MNRAS, 377, 1557
Norberg, P., Baugh, C. M., Gaztañaga, E., & Croton, D. J. 2009, MNRAS, 396, 19
Oliver, S. J., Bock, J., Altieri, B., et al. 2012, MNRAS, 424, 1614
Pascale, E., Auld, R., Dariush, A., et al. 2011, MNRAS, 415, 911
Pérez, F. & Granger, B. E. 2007, Computing in Science and Engineering, 9, 21
Pilbratt, G. L., Riedinger, J. R., Passvogel, T., et al. 2010, A&A, 518, L1
Planck Collaboration, Aghanim, N., Akrami, Y., et al. 2020, A&A, 641, A6
Poglitich, A., Waelkens, C., Geis, N., et al. 2010, A&A, 518, L2
Rigby, E. E., Maddox, S. J., Dunne, L., et al. 2011, MNRAS, 415, 2336
Sarkar, S., Pandey, B., & Khatri, R. 2019, MNRAS, 483, 2453
Schneider, P., Ehlers, J., & Falco, E. E. 1992, Gravitational Lenses
Scranton, R., Ménard, B., Richards, G. T., et al. 2005, ApJ, 633, 589
Shao, J. 1986, The Annals of Statistics, 14, 1322
Sureshkumar, U., Durkalec, A., Pollo, A., et al. 2021, A&A, 653, A35
The Dark Energy Survey Collaboration. 2005, arXiv e-prints, astro
Valiante, E., Smith, M. W. L., Eales, S., et al. 2016, MNRAS, 462, 3146
Wardlow, J. L., Cooray, A., De Bernardis, F., et al. 2013, ApJ, 762, 59
Zehavi, I., Zheng, Z., Weinberg, D. H., et al. 2005, ApJ, 630, 1